

Experimental Study on the Wake Meandering Within a Scale Model Wind Farm Subject to a Wind-Tunnel Flow Simulating an Atmospheric Boundary Layer

Nicolas Coudou^{1,2,3} · Sophia Buckingham¹ · Laurent Bricteux² · Jeroen van Beeck¹

Received: 31 October 2016 / Accepted: 31 October 2017 / Published online: 6 December 2017
© Springer Science+Business Media B.V., part of Springer Nature 2017

Abstract The phenomenon of meandering of the wind-turbine wake comprises the motion of the wake as a whole in both horizontal and vertical directions as it is advected downstream. The oscillatory motion of the wake is a crucial factor in wind farms, because it increases the fatigue loads, and, in particular, the yaw loads on downstream turbines. To address this phenomenon, experimental investigations are carried out in a wind-tunnel flow simulating an atmospheric boundary layer with the Coriolis effect neglected. A 3×3 scaled wind farm composed of three-bladed rotating wind-turbine models is subject to a neutral boundary layer over a slightly-rough surface, i.e. corresponding to offshore conditions. Particle-image-velocimetry measurements are performed in a horizontal plane at hub height in the wakes of the three wind turbines occupying the wind-farm centreline. These measurements allow determination of the wake centrelines, with spectral analysis indicating the characteristic wavelength of the wake-meandering phenomenon. In addition, measurements with hot-wire anemometry are performed along a vertical line in the wakes of the same wind turbines, with both techniques revealing the presence of wake meandering behind all three turbines. The spectral analysis performed with the spatial and temporal signals obtained from these two measurement techniques indicates a Strouhal number of $\approx 0.20 - 0.22$ based on the

✉ Nicolas Coudou
nicolas.coudou@vki.ac.be

Sophia Buckingham
sophia.buckingham@vki.ac.be

Laurent Bricteux
Laurent.BRICTEUX@umons.ac.be

Jeroen van Beeck
vanbeeck@vki.ac.be

¹ Environmental and Applied Fluid Dynamics Department, von Karman Institute for Fluid Dynamics, Waterloosesteenweg 72, 1640 Sint-Genesius-Rode, Belgium

² Fluids-Machines unit, Polytechnic Faculty, University of Mons (UMONS), Rue du Joncquois 53, 7000 Mons, Belgium

³ Institute of Mechanics, Materials and Civil Engineering, Université catholique de Louvain (UCL), Place du Levant 2, 1348 Louvain-la-Neuve, Belgium

characteristic wake-meandering frequency, the rotor diameter and the flow speed at hub height.

Keywords Wind-tunnel-scale atmospheric boundary layer · Hot-wire anemometry · Particle image velocimetry · Wake meandering · Wind-turbine wakes

1 Introduction

Between the years 2000 and 2015, the cumulative wind-power installations in the European Union increased from 12.9 GW to 141.6 GW (Corbetta et al. 2016) and, based on the European Wind Energy Association's central scenario (Corbetta et al. 2015), wind-energy installations are predicted to generate 320 GW by 2030. Hence, with the rise in the use of wind energy, more and larger clustered wind farms are expected to appear. An important aspect of a wind-farm design is the optimization of the wind-farm layout, which consists in optimally positioning the wind turbines within the wind farm, so that the wake effects are minimized and, therefore, the efficiency and lifetime of downstream turbines are maximized. This requires an in-depth knowledge of wind-turbine wakes, and, especially, a better understanding of the well-known but less understood wake-meandering phenomenon. Because this phenomenon causes the wake to be swept in and out of the rotor disk of downstream turbines, a considerable increase occurs in the fatigue and, particularly, yaw loading of these turbines.

Two main possible reasons for the formation of wake meandering have been suggested over the past few years. First, the intrinsic instabilities of the wake associated with a periodic vortex shedding within the wake (España et al. 2012), the rotor swept disk of the wind turbine acting as a porous bluff body with decreasing permeability as the tip-speed ratio increases. Second, the effects of the large-scale turbulent eddies contained in the atmospheric boundary layer (ABL) as observed for plume-dispersion analysis (España et al. 2012).

The experiments of Medici and Alfredsson (2006) using a scaled model of a two-bladed rotating wind turbine subject to a uniform freestream flow suggest the role of intrinsic instabilities. Medici and Alfredsson (2006) argued that the low-frequency vortex shedding may be responsible for the wake-meandering motion. Their measurements were since supported by the theoretical study of Okulov and Sørensen (2007). However, as mentioned in Larsen et al. (2008), notable differences exist between the experimental conditions of Medici and Alfredsson (2006), and the conditions present for a full-scale wind turbine located in the ABL. Medici and Alfredsson (2008) further complemented earlier studies of the meandering of wind-turbine wakes by investigating the influence of the number of blades, the blade pitch angle and the tip-speed ratio on the meandering frequency. Their measurements show that the Strouhal number

$$St = \frac{fD}{U_{hub}}, \quad (1)$$

based on the characteristic wake-meandering frequency f , the rotor diameter D and the freestream wind speed at hub height U_{hub} , varies between 0.1 and 0.3 depending on the operating conditions.

España et al. (2012) assumed that small-scale eddies (i.e. smaller than the rotor diameter) constituting the high-frequency part of the turbulence spectrum are responsible for diffusive effects in the wake only, whereas the low-frequency part composed of eddies larger than the rotor diameter acts to transport the wake as a whole (España et al. 2012). The wake-meandering process can, therefore, be described as a series of consecutive wake “releases”,

each advected downstream with the mean velocity field and displaced by the large-scale turbulent structures in the plane perpendicular to the mean flow direction. In relation to the large-scale turbulent structures, the individual wake “releases” are thus presumed to behave like passive tracers (Larsen et al. 2008). Experimental evidence of the role of large eddies on the wake-meandering phenomenon behind a wind turbine modelled with a static porous disk has been provided by Aubrun et al. (2011) and España et al. (2011, 2012). Experiments performed in both neutral stability, and homogeneous and isotropic turbulence conditions, show that the meandering process is only generated for turbulent length scales larger than the disk diameter, and that the meandering phenomenon, characterized by random oscillations of the wake, cannot be attributed to periodic vortex shedding.

Chamorro et al. (2013) provided evidence of wake meandering for a hydrokinetic turbine located in a turbulent boundary layer. Their acoustic Doppler velocimetry measurements show that, at distances greater than three rotor diameters, the wake has a strong lateral periodic motion of low frequency corresponding to $St = 0.28$ at $x/D = 4$. From laser Doppler anemometry measurements performed in the wake of a three-bladed wind-turbine rotor located in a water flume, Okulov et al. (2014) found that the wake oscillates periodically with $St \approx 0.23$, independent of the operating conditions.

The experiments of Muller et al. (2015) and Aubrun et al. (2015) using static porous disks located in a neutral boundary layer show that, while the instantaneous horizontal wake position correlates well with the upstream transverse velocity component for wavelengths larger than three times the disk diameter, this is not true for wavelengths smaller than twice the disk diameter. They argued that the lateral force is a better candidate than the upstream transverse velocity component for predicting the real-time meandering process, since the coherent frequency range between the position of the wake and the lateral force is wider than that for the coherence with the upstream transverse velocity component (Muller et al. 2015). Finally, using two porous disks located $5D$ apart from each other, an amplification of the wake meandering for the downstream turbine was observed due to the upstream wake.

From particle-image-velocimetry (PIV) measurements performed in the wake of two rotating three-bladed scale models placed in a neutral boundary layer, Howard et al. (2015) reported that the velocity deficit in the wake, resulting from specific turbine operating conditions, appears to be a key governing parameter for meandering. Indeed, they noted that a larger velocity deficit compresses the wake meandering in both horizontal directions. Moreover, they observed large-scale oscillations corresponding to $St \approx 0.3$ for a wind-turbine scale model operating at an optimal tip-speed ratio.

The wake of a three-bladed rotating wind-turbine scale model in onshore (moderately rough) and offshore (slightly rough) neutral boundary-layer conditions has been investigated by Barlas et al. (2016). For offshore conditions, i.e. low turbulence intensity ($I = \sigma_u/U_{hub} = 7.5\%$ at hub height, where σ_u is the standard deviation of the freestream velocity component), a wake-meandering mechanism was detected through a low-frequency peak in the turbulent energy spectrum. It was found that the Strouhal number related to this meandering is always ≈ 0.25 , which is a typical value for bluff-body vortex shedding (Sumer and Fredsøe 1997). Additional investigations were performed in offshore and onshore conditions downstream of a 3×3 wind farm, but, as for the single wind turbine in onshore conditions ($I = 17.5\%$ at hub height), the incoming turbulence intensity was too high for the meandering to survive (Barlas et al. 2015).

While most of the experimental studies on meandering of the wind-turbine wake concern an isolated wind-turbine scale model or two models aligned with the mean flow in a few cases, the current study focusses on the three wind turbines of the middle row (in the streamwise direction) of a 3×3 scaled wind farm. Rotating scale models of three-bladed wind turbines

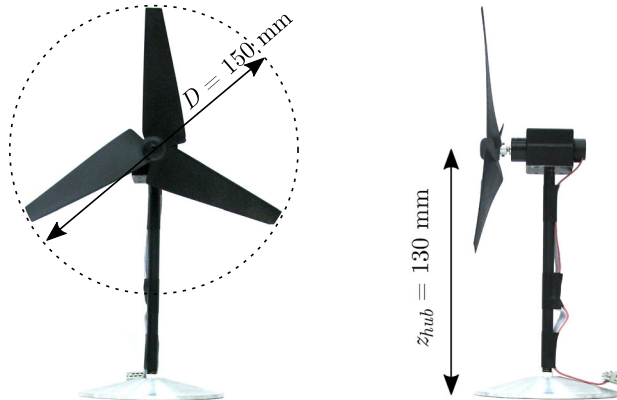


Fig. 1 Wind-turbine scale model dimensions

enable more realistic flow dynamics (tip vortices and rotational momentum) than porous disks. Furthermore, since each model is equipped with a generator, the power produced by the turbines can be measured. In particular, our aim is to extend the study of Barlas et al. (2015) by investigating whether the wake meandering persists in a scaled wind farm placed in a neutral boundary layer corresponding to a slightly-rough terrain (offshore conditions) in the atmosphere, and to determine the characteristics of this phenomenon. This is accomplished using state-of-the-art experimental techniques combined with spectral analysis.

2 Experimental Set-Up

2.1 Wind-Turbine Scale Model

The three-bladed wind-turbine scale models used for the experiments have a rotor diameter of 0.15 m and a hub height of 0.13 m (Fig. 1). The scale-model dimensions make it possible to position a 3×3 wind farm in our wind tunnel (see Sect. 2.3), and are well adapted to obtaining integral length scales larger than the wind-turbine rotor diameter.

The rotors were designed based on blade-element momentum theory (Burton et al. 2001), with optimization of the power coefficient C_p for an incoming flow speed of 8 m s^{-1} at hub height. To deal with the low Reynolds numbers for the scale models ($Re \leq 27 \times 10^3$, based on the chord length and relative velocity for each blade element), the rotors were made of a thin airfoil (i.e. the HAM-STD HS1-606 airfoil). The main characteristics of the wind-turbine blades can be found in Table 4 (“Appendix 1”). The rotors were manufactured by three-dimensional printing; each rotor is attached to a direct-current motor located inside the nacelle and used as a generator, which can be “counter-loaded” by connecting it to an electrical circuit to extract power from the incoming flow. By varying the resistance of the circuit, the resistance of the generator is changed, which enables the control of the turbine angular velocity Ω , and, therefore, the turbine tip-speed ratio

$$TSR = \frac{\Omega R}{U_{hub}}, \quad (2)$$

where U_{hub} is the mean flow speed at hub height, and R is the rotor radius. Based on the incoming flow speed at hub height ($U_{hub} = 8.3 \text{ m s}^{-1}$), the tip-speed ratio of the first turbine is equal to 7.2.

The scale-model dimensions are representative of a 2-MW offshore wind turbine (e.g. scale 1/440 of a Vestas V66-2MW wind turbine), and given the large scaling factor, it was determined whether the results of our scaled experiments could be extrapolated to full-scale wind turbines. According to Chamorro et al. (2012), the Reynolds-number independence for higher-order statistics (i.e. turbulence intensity and kinematic shear stress) starts at $Re \approx 9.3 \times 10^4$, while the mean-velocity deficit (lower-order statistics) already becomes insensitive to Reynolds-number effects at $Re = U_{hub}D/\nu \approx 4.8 \times 10^4$, with D the wind-turbine rotor diameter and ν the kinematic viscosity. For our scale model, the Re influence was investigated by comparing the mean velocity and turbulence-intensity profiles obtained from PIV measurements at hub height in the wake of the model at $Re = 5 \times 10^4$ and $Re = 8.5 \times 10^4$ (Fig. 2). The Reynolds-number independence for the mean velocity is already reached at $Re = 5 \times 10^4$, which is in agreement with the reference Re for independence of lower-order statistics reported by Chamorro et al. (2012). Concerning the turbulence-intensity profiles, with a change in I (Eq. 7b) of less than 2% observed between $Re = 5 \times 10^4$ and $Re = 8.5 \times 10^4$, it is expected that Re independence for the turbulence intensity is close to the reference Re for the independence of higher-order statistics reported by Chamorro et al. (2012). Therefore, for the highest Re reached during our experiments ($Re = 8.5 \times 10^4$), Re independence is reached for the main flow statistics.

2.2 Wind-Farm Set-Up

The 3×3 wind farm was located at the end of the test section of the von Karman Institute's L-1B wind engineering facility (Fig. 3). The wind-turbine scale models were separated by distances of $3D$ and $5D$ in the spanwise and streamwise directions, respectively, which are representative of a full-scale wind farm, and were also used in Barlas et al. (2015), thus enabling comparison of the results between both studies.

Due to the limitations in the positioning of the PIV camera underneath the wind tunnel (see Sect. 2.4.1), the PIV system remained stationary, while the wind farm was shifted longitudinally for successive measurements in the wake of the first, second and third turbines as depicted in Fig. 3. These changes in wind-farm positioning have no influence on the reliability of the results, since the entire testing area is contained within a fully-developed boundary layer. Furthermore, since the PIV system remains in the same position, the comparison of the wind-turbine wakes is not affected by changes in the PIV set-up.

2.3 Boundary-Layer Modelling in the L1-B Wind Tunnel

The L-1B wind tunnel of the von Karman Institute for Fluid Dynamics is a low-speed, closed-loop wind tunnel with a 2-m high, 3-m wide, and 20-m long test section. Different floors with variable roughness elements enable the growth and control of a turbulent boundary layer similar to the lower part of the neutral ABL, with the Coriolis effect neglected. Based on Barlas et al. (2015, 2016), a neutral boundary layer corresponding to a slightly rough terrain (offshore conditions) was modelled for the experiments. To initialize the neutral boundary layer, a 0.15-m high fence and a monoplane grid with a mesh size of $0.02 \text{ m} \times 0.02 \text{ m}$ were located at the beginning of the test section containing no roughness elements. The length of the flow-development section was equal to 11 m for the shortest scenario, corresponding to the wind farm in configuration 3, which is sufficiently long for the establishment of a

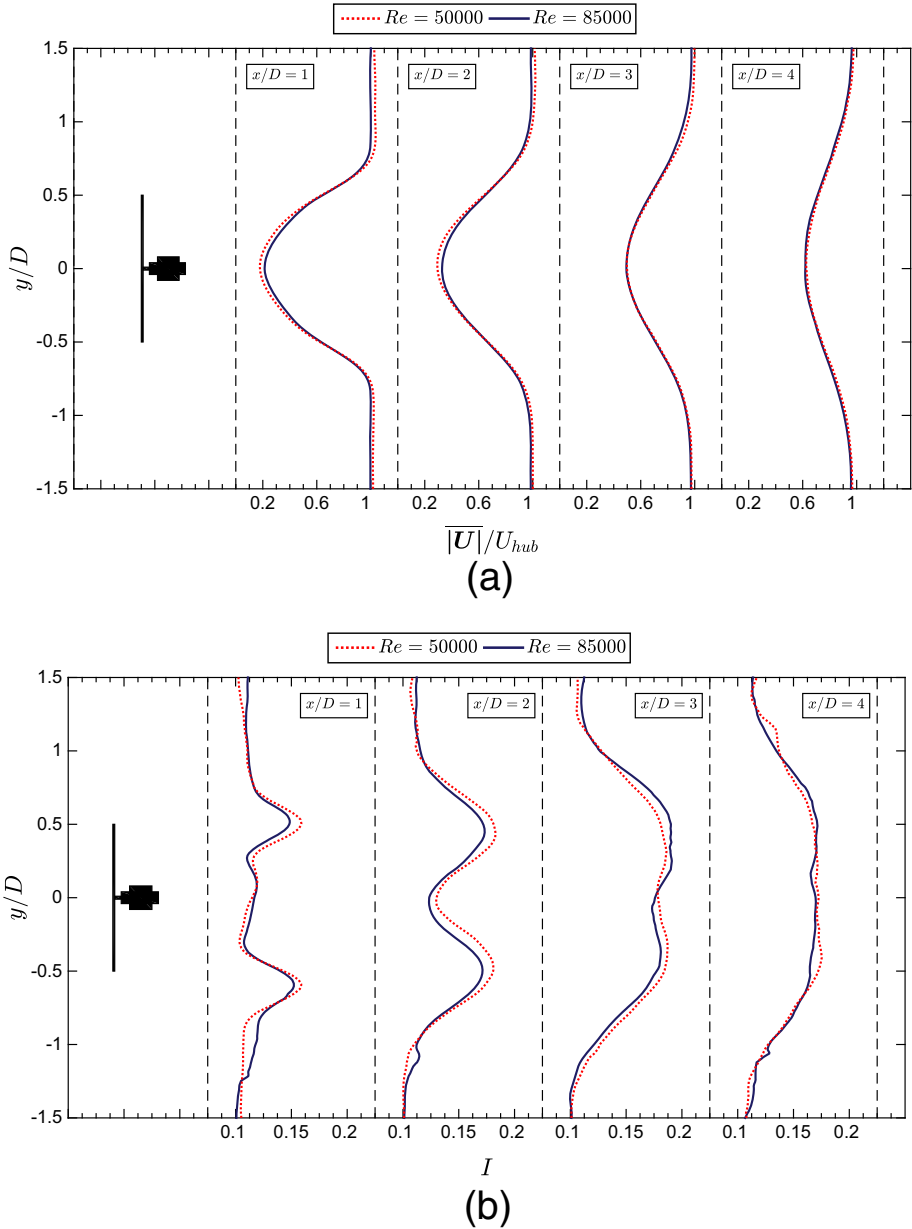


Fig. 2 Normalized velocity (a), and turbulence-intensity (b) profiles at hub height for $Re = 5 \times 10^4$ and $Re = 8.5 \times 10^4$

fully-developed boundary layer. More information concerning the modelling of atmospheric flows in the L-1B wind tunnel is found in Buckingham (2010) and Conan (2012).

After verification of the lateral homogeneity of the flow inside the PIV field-of-view, the boundary layer modelled in the wind tunnel was characterized using a one-component hot-wire anemometer. The measurements were performed along a vertical line located in

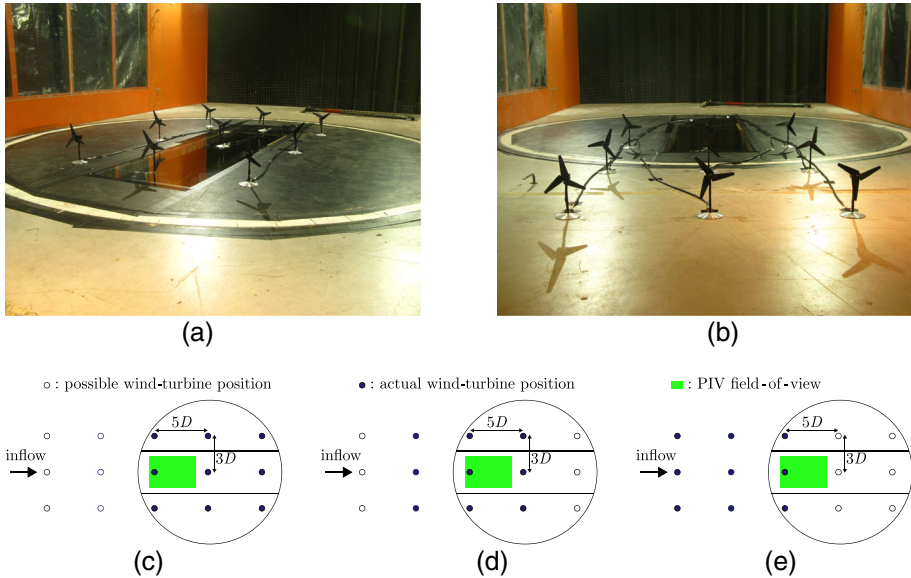


Fig. 3 Wind-farm location in the L-1B wind engineering facility of the von Karman Institute for Fluid Dynamics. Photograph of configurations 1 (a) and 3 (b), and sketches of configurations 1 (c), 2 (d) and 3 (e)

the rotor plane of the first wind turbine of the wind farm in configuration 1 (Fig. 3c). From 10 mm to 320 mm, measurements were taken every 10 mm. For each location, the hot-wire-anemometry signal was acquired for 120 s with a sampling frequency of 3 kHz and filtered at 1 kHz. It is important to note that, despite the fact that the hot wire was positioned to measure the streamwise velocity component, the velocity acquired with one-component hot-wire anemometry is not the streamwise velocity component, but strictly the effective velocity.

From the measured velocity profile, parameters corresponding to the logarithmic law

$$\frac{U}{u_*} = \frac{1}{\kappa} \ln\left(\frac{z - d_0}{z_0}\right) \tag{3}$$

and power law

$$\frac{U}{U_{ref}} = \left(\frac{z - d_0}{z_{ref} - d_0}\right)^\alpha \tag{4}$$

are determined by fitting the experimentally-averaged velocity profile in a semi-logarithmic and logarithmic-logarithmic plot, respectively. Here, U is the mean horizontal flow speed, u_* is the friction velocity, κ is the von Karman constant, z is the height above the surface, z_0 is the aerodynamic roughness length, which is a function of the real surface roughness, $d_0 \approx 0$ is the zero-plane displacement, α is the power-law coefficient, and U_{ref} corresponds to the velocity at a reference height z_{ref} , which was set as the hub height.

Table 1 presents these modelled parameters. After scaling the aerodynamic roughness length to its full-scale value ($z_{0f,s} = 440 z_{0wt,s}$), these parameters were compared to various engineering guidelines (VDI Guidelines 3783/12 2000; Eurocode 2005; ESDU 1985). According to these guidelines, the values of the parameters obtained correspond to the upper limit of the *slightly rough* roughness class representing an ice, snow or water “terrain” (ter-

Table 1 Parameters with their uncertainty bounds for the logarithmic law and the power law for the modelled boundary layer in the L-1B wind tunnel

u_* (m s ⁻¹)	0.330 ± 0.015
$z_{0_{wind\ tunnel\ scale}}$ (m)	$5.5 \times 10^{-6} < 8.4 \times 10^{-6} < 12.8 \times 10^{-6}$
$z_{0_{full\ scale}}$ (m)	$2.4 \times 10^{-3} < 3.7 \times 10^{-3} < 5.6 \times 10^{-3}$
α	0.113 ± 0.005

rain category of *type 0* according to the Eurocode standard (Eurocode 2005)). Based on these standards, it can be concluded that a neutral boundary layer representing offshore conditions is modelled in the L-1B wind tunnel.

Figure 4a, c presents the measured vertical profiles of the normalized mean velocity $U(z)/U_{hub}$, the turbulence intensity $I(z) = \sigma(z)/U(z)$, where σ is the standard deviation of the streamwise velocity component, and the normalized integral length scales $L(z)/D$ in the streamwise direction. The mean velocity profile is compared with the logarithmic law (Eq. 3) and the power law (Eq. 4). The turbulence-intensity profile is compared with the limits for a slightly-rough terrain corresponding to $10^{-5} \text{ m} < z_0 < 5 \times 10^{-3} \text{ m}$, as suggested by the VDI Guidelines 3783/12 (2000). The integral length scales (L) are computed by applying the autocorrelation method to the time series and invoking Taylor's frozen turbulence hypothesis. Due to a lack of information in these guidelines concerning the integral length scales, the limits were computed based on the ESDU guidelines (ESDU 1985), with $10^{-5} \text{ m} < z_0 < 5 \times 10^{-3} \text{ m}$. The integral length scale at hub height appears to be about three rotor diameters, which is the characteristic size of the energy-containing eddies corresponding to the conditions presented in España et al. (2011, 2012), where the wake-meandering phenomenon requires turbulent scales in the inflow larger than the wind-turbine rotor diameter.

A usual representation of the distribution of energy for atmospheric flows is the neutral Kaimal spectrum (Kaimal and Finnigan 1994), which is the energy spectrum normalized by the frequency and the square of the friction velocity ($fS(f)/u_*^2$), where a reduced frequency $n = fz/U$ based on the height z and mean velocity at that height, is used. The Kaimal spectrum for the streamwise velocity component (Kaimal and Finnigan 1994) is given by

$$\frac{fS(f)}{u_*^2} = \frac{102n}{(1 + 33n)^{\frac{5}{3}}}. \quad (5)$$

The normalized turbulent spectrum obtained at hub height compares well with the Kaimal spectrum in Fig. 4d, but with a slight overshoot in the amplitude of the peak, which is consistent with Conan (2012). This overshoot is most probably caused by a low-frequency instability ($f \approx 1.5 \text{ Hz}$) produced by the two counter-rotating fans of the wind tunnel. Note that this frequency is about ten times smaller than the meandering frequency.

2.4 Measurement Techniques

2.4.1 Particle Image Velocimetry

The 2D2C-PIV technique was used to perform measurements in a horizontal plane at hub height in the wake of the wind-turbine scale models. Therefore, the laser was positioned on one side of the test section, with the CCD camera (Imager SX 4M) located below the test section, and recording images through a flush-mounted Plexiglas window in the turntable of

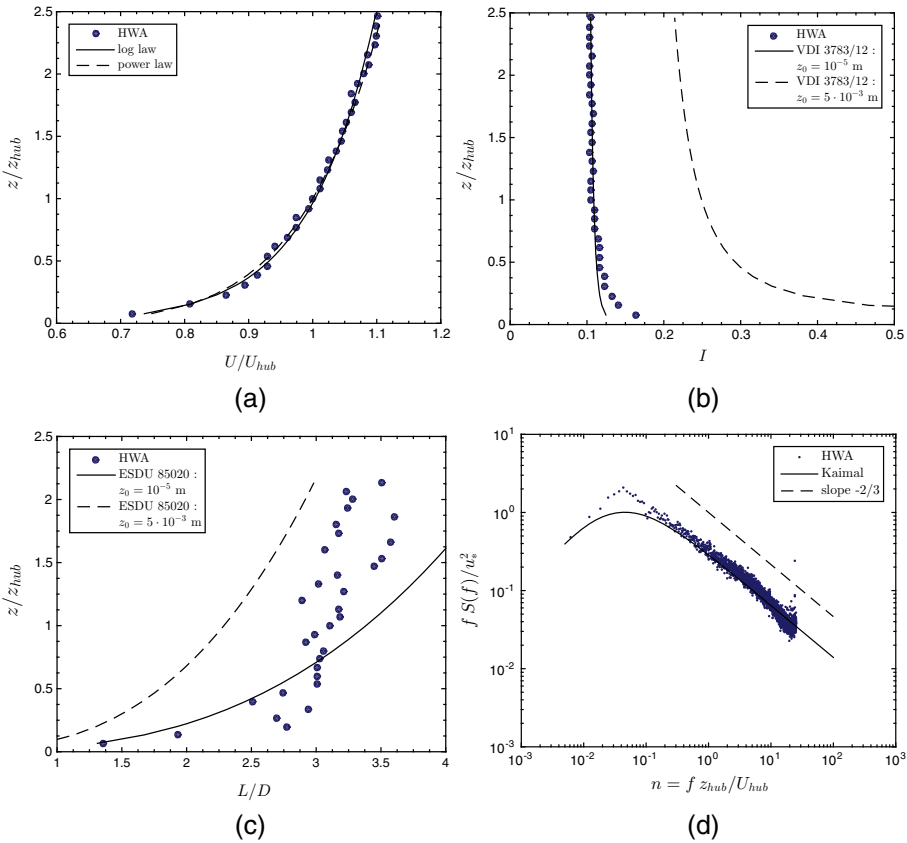


Fig. 4 Vertical profiles and normalized spectrum of the modelled boundary layer in the L-1B wind tunnel. The normalized mean velocity (a), turbulence intensity (b), integral length scales (c), normalized spectrum at hub height and Kaimal spectrum (Kaimal and Finnigan 1994) (d). Note that all the statistics are based on the streamwise velocity component

the wind tunnel (Fig. 5). The camera has a spatial resolution of four megapixels, was equipped with a 35-mm Nikkor lens, and was located at approximately 2 m from the laser sheet to obtain a field-of-view larger than $4D$ in the streamwise direction. To collect a large amount of light scattered by the seeding particles, the aperture was set to $f_{\#} = 2.8$. The seeding particles are oil droplets of diameter of $1-5 \mu\text{m}$, produced by a smoke generator composed of a plate heated at 180°C on which oil is vaporized. To obtain a uniform seeding, the oil particles were injected into the end of the test section so that mixing aided by the counter-rotating fans occurs in the return circuit of the wind tunnel. Measurements were performed using LaVision's DAVIS 8 software. Two cavities of a Nd-Yag pulsed laser were used to obtain two flashes of light separated by a fixed time of $\Delta t = 290 \mu\text{s}$ for $U_{hub} = 8.3 \text{ m s}^{-1}$ and $\Delta t = 470 \mu\text{s}$ for $U_{hub} = 4.9 \text{ m s}^{-1}$, resulting in particle displacements of about eight pixels. For each measurement, 800 image pairs were acquired at a frequency of 2.5 Hz to provide statistically independent quantities for computation of the mean velocity and the standard deviation. The processing of the images was carried out using in-house software (Scarano 2000) with 64×64 -pixel interrogation areas, and an overlap of 75%. For all fields-of-view, the signal-to-noise ratio is approximately six, giving confidence in the quality of

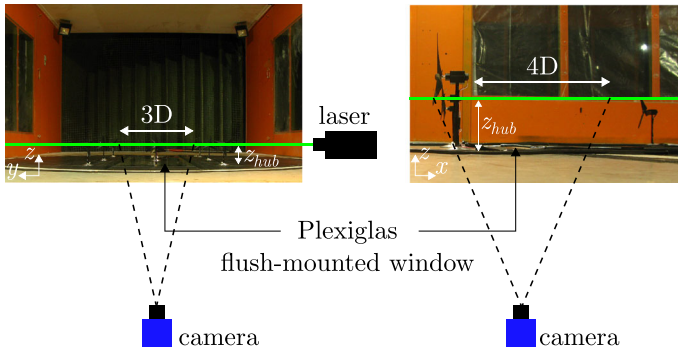


Fig. 5 PIV set-up in the L-1B wind tunnel

the measurements and processing. Based on the uncertainty analysis procedure proposed by the [International Towing Tank Conference \(2008\)](#), and considering a confidence interval of 95%, the uncertainties in the mean and standard deviation of the velocity are 1.5% and 2.5%, respectively.

2.4.2 Hot-Wire Anemometry

The hot-wire anemometer was calibrated using a low-turbulent, uniform jet created by a nozzle and controlled by a pressure difference. The calibration was carried out before and after each experimental campaign to verify the validity of the calibration throughout the experiments. The calibration curve was then fitted with a third-order polynomial for converting the instantaneous voltage signature into an instantaneous flow. The measurements in the wind-turbine wakes were performed at $x = 2D$ downstream of each rotor disk for heights ranging between $z = 30$ mm and $z = 320$ mm in increments of 10 mm, as well as at the lower and upper blade-tips heights. For each location, the hot-wire-anemometry signal was acquired for a duration of 120 s, with a sampling frequency of 3 kHz, and low-pass filtered at 1 kHz. Based on classical uncertainty analysis ([Anthoine et al. 1994](#)) and considering a confidence interval of 95%, the uncertainty is 4.1% for a hub-height flow speed of 7.8 m s^{-1} . Note that, even if the use of a single hot wire within a wake is questionable, it was sufficient for the present objective of acquiring power spectra for the determination of the wake-meandering frequency.

3 Estimation of the Wake Centre

From the PIV measurements of the scaled wind-turbine wakes, a specific processing technique is used to determine the instantaneous deviations of the wake-centre position from its time-averaged location. A processing technique applied to the instantaneous velocity fields, and based on the determination of the wake-deficit borders through a threshold value based on the external velocity of the flow ($U_{th} = 0.95 U_{ext}$) was tested by [España et al. \(2011\)](#). However, the high turbulence intensity contained in the flow leads to very noisy velocity fields, making the determination of the instantaneous borders of the wake deficit both difficult and uncertain ([España et al. 2011](#)).

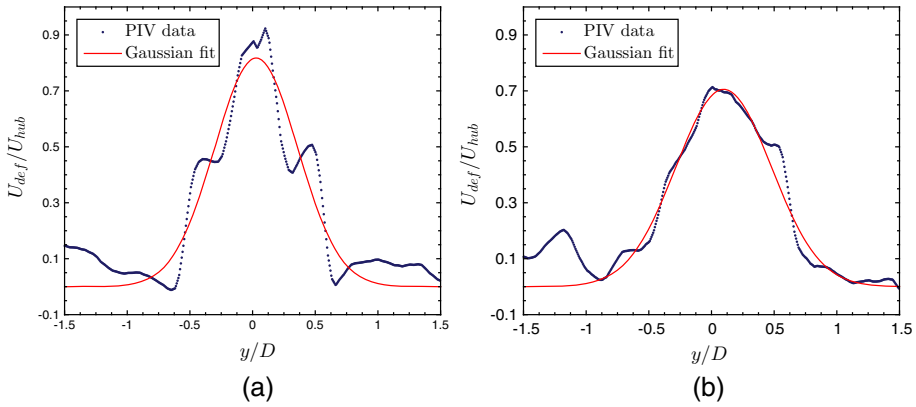


Fig. 6 Gaussian fit of two profiles of the normalized instantaneous wake velocity deficit ($U_{def} = U_{free\ stream} - U_{wake}$) at hub height for $x = 0.5D$ (a) and $x = 3D$ (b)

An alternative approach detailed in Bingöl et al. (2010), and used in Aubrun et al. (2012) and Vollmer et al. (2016), is based on the determination of a Gaussian profile fitted to the instantaneous wake velocity deficit

$$f(y) = \frac{A}{2\pi\sigma} \exp\left(-\frac{(y_i - \mu_y)^2}{2\sigma^2}\right). \tag{6}$$

The independent Cartesian spatial variable of the function is referred to as y_i and the shape of the function is parametrized in terms of the position parameter of the profile μ_y , the width parameter of the profile σ , and a scaling parameter A (Vollmer et al. 2016).

The fitting procedure is performed as follows. For each snapshot, the Gaussian function defined by Eq. 6 is fitted to the instantaneous velocity-deficit profiles at hub height (Fig. 6) for the streamwise locations x_i from $x = 0.5D$ to $x = 4D$. For each position x_i , the Gaussian function is fitted using a least-squares approach, with A bounded on $[0, \infty]$, μ_y on $[-1.5D, 1.5D]$, and σ_y on $[0, 2D]$. The wake-centre position at each location x_i is then determined from the location of the maximum of the fitted Gaussian function to each velocity-deficit profile.

4 Results and Discussion

4.1 Wake-Meandering Characteristics from Particle-Image-Velocimetry Fields

The results presented here are obtained from PIV measurements performed in a horizontal plane at hub height in the wake of the three wind turbines in the middle row (in the streamwise direction) of the wind farm. The horizontal velocity and the turbulence intensity presented in the figures below are computed as

$$|U| = \sqrt{u^2 + v^2} \tag{7a}$$

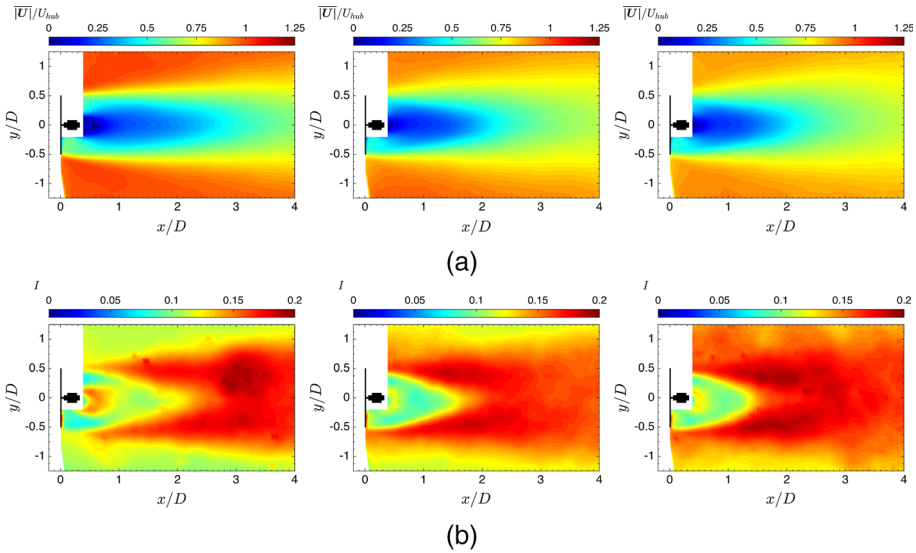


Fig. 7 Normalized average velocity (a) and turbulence intensity fields (b) at hub height for the first (left), second (centre) and third (right) turbines

and

$$I = \frac{\sqrt{\frac{u'^2 + 2v'^2}{3}}}{U_{hub}}, \quad (7b)$$

respectively, where u and v are the instantaneous streamwise and lateral velocity components, respectively, and a prime denotes a fluctuation.

Figure 7a shows the average velocity fields, which reveal the extension of the wake of the first wind turbine further downstream than the wakes of the second and third turbines. The faster wake recovery of the latter two turbines results from the higher turbulence intensity of the wake-disturbed inflow compared with the undisturbed inflow reaching the first wind turbine. Indeed, the mechanical turbulence created by the upstream turbine(s) (Fig. 7b) enhances the mixing of the low-velocity fluid in the wake with the undisturbed high-velocity fluid outside of it, resulting in the increased transfer of momentum into the wake, which reduces the velocity deficit and, consequently, the distance over which the wake recovers.

The difference in flow velocities inside and outside the wake results in the formation of turbulent eddies within a shear layer, which thickens downstream (Fig. 7b) until reaching the wake axis, and marking out the end of the near-wake region. The near-wake region extends from the turbine rotor disk to approximately $2.75D$, $2.2D$, and $2.1D$ downstream of the first, second, and third turbines, respectively.

The wake extension has a direct impact on the power produced, which for the second turbine is about 55% of the power produced by the first turbine, and for the third turbine is about 58% of the power of the first turbine. This slight increase for the third turbine results from the faster wake recovery behind the second turbine compared with that of the first turbine (Fig. 7a), consistent with other wind-tunnel (Barlas et al. 2015) and field experiments (Churchfield et al. 2015).

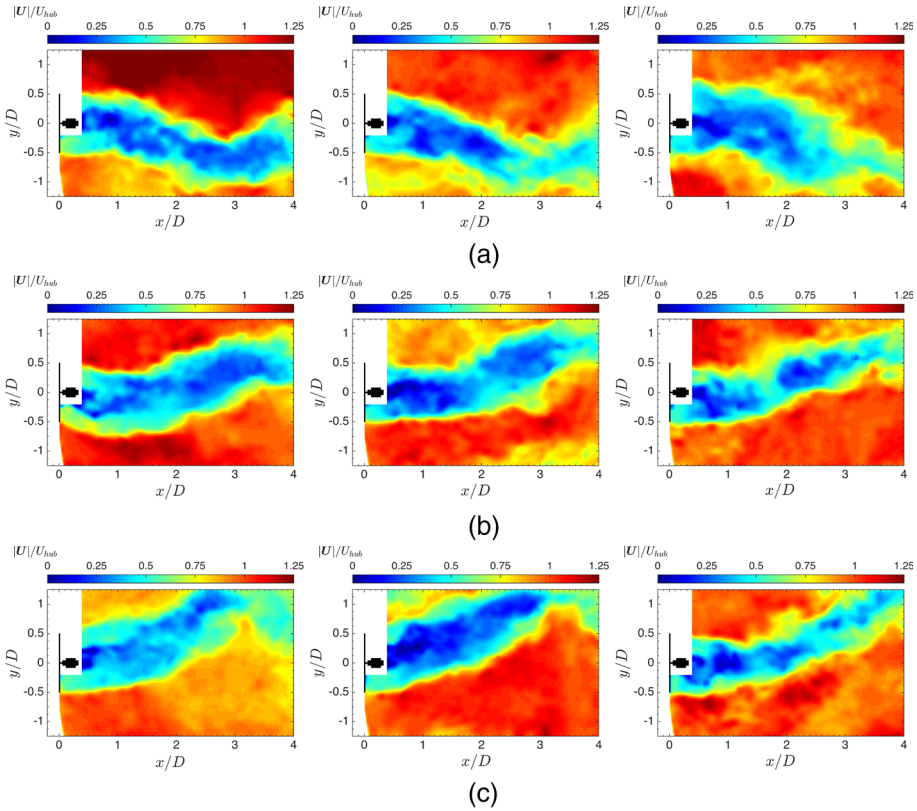


Fig. 8 Normalized instantaneous velocity fields at hub height at three different times (a, b, c) revealing wake deflection for the first (left), second (centre) and third (right) turbines

Normalized instantaneous velocity fields at hub height (Fig. 8) clearly highlight the wake-meandering phenomenon that, in contrast to the results of Barlas et al. (2015), persists inside the wind farm, and is clearly still present beyond the first two rows. The different meandering behaviours follow from the difference between the two experimental campaigns, including (i) the wind-turbine rotor, (ii) the tip-speed ratio, and (iii) the boundary-layer properties. While both rotors are based on very similar airfoils (Fig. 9), ours is slightly thicker than the GM15 airfoil of Barlas et al. (2015) for $0.4 \leq x/c \leq 1$. This is to avoid the very high costs and poor quality of three-dimensional printing, and then the additional manufacturing needed for the thinnest airfoil. While both rotor designs are based on the blade-element-momentum method described in Burton et al. (2001), and are thus similar, the differences between the two rotors cannot justify the different meandering behaviours observed. Barlas et al. (2015, 2016) have shown that the Strouhal number corresponding to the meandering frequency is ≈ 0.25 for a tip-speed ratio ranging from 5 and 7.75. Since our tip-speed ratios fall within this range, this also cannot justify the different meandering behaviour. Therefore, the difference is most probably due to the higher turbulence intensity of the inflow here ($I = 10.5\%$ at hub height) compared with that ($I = 7.5\%$ at hub height) of Barlas et al. (2015). The major influence of the turbulence intensity on the meandering is confirmed by the fact that, in Barlas et al. (2015, 2016), the absence of meandering is observed in the wake of a single wind turbine

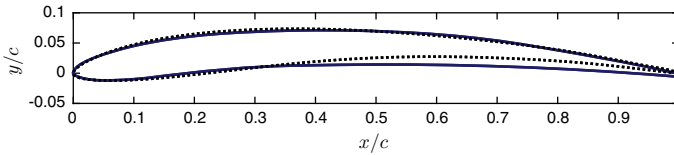


Fig. 9 Comparison between our airfoil (HAM-STD HS1-606) (continuous line) and that (GM15) of Barlas et al. (2015, 2016) (dotted line)

located in a rough-terrain boundary layer of very high turbulence intensity ($I = 17.5\%$ at hub height).

Figure 10a, b show an instantaneous wake width of the downstream turbines often clearly larger than one rotor diameter directly behind the rotor ($x/D = 0$). Because of wake meandering, the wake of upstream turbines asymmetrically impacts the rotor of downstream turbines, which highlights the problem of wake meandering inside wind farms.

Less than 10 of the 2400 acquired instantaneous velocity fields reveal a possible interaction between the wakes of the lateral rows, and those of the central row of turbines (Fig. 10c). Therefore, it is not possible to draw a firm conclusion about the lateral interactions of the wakes without additional data, which is the purpose of future experiments.

Normalized vorticity fields corresponding to the instantaneous normalized velocity fields of Fig. 8a, b are presented in Fig. 11. As the blade-tip vortices following a helical path with rotation opposite to the rotor are clearly visible, the wake boundaries can easily be determined. Furthermore, the tip vortices become disorganized through the wind farm due to the increased overall turbulence intensity.

As described above, the wake position as a function of the streamwise position is obtained by locating the maximum of the fitted Gaussian functions to the instantaneous wake velocity deficits at hub height. Figure 12 presents the instantaneous normalized wake-centre positions as a function of the streamwise location at hub height for each instantaneous velocity field. The wake-centre displacements in the y -direction sometimes reach the limit of the field-of-view of the camera. These “extreme deflections” of the wake are evident in Fig. 8c.

For each wake-centre-position curve, a fast Fourier transform is applied, after subtraction of the mean position and zero-padding, to obtain the characteristics of the wake-meandering phenomenon. Since the fast Fourier transform is applied on a spatial signal, the resulting spectrum is obtained as a function of the wavenumber k or the wavelength $\lambda = k^{-1}$. By applying Taylor’s frozen turbulence hypothesis, the spectrum is then expressed as a function of the frequency

$$f = \frac{U_{hub}}{\lambda}, \quad (8)$$

and subsequently of the Strouhal number

$$St = \frac{fD}{U_{hub}} = \frac{D}{\lambda}. \quad (9)$$

To investigate the influence of the incoming flow speed on the meandering phenomenon, the same methodology is applied for measurements performed for a flow speed of 4.9 m s^{-1} at hub height. The average spectra of the wake-centre position as a function of the Strouhal number, and of the frequency normalized by the wind-turbine frequency (Table 2), are shown in Fig. 13. The wake-meandering characteristics obtained from the spectra are summarized in Table 3. The characteristic Strouhal numbers and normalized frequencies match well with

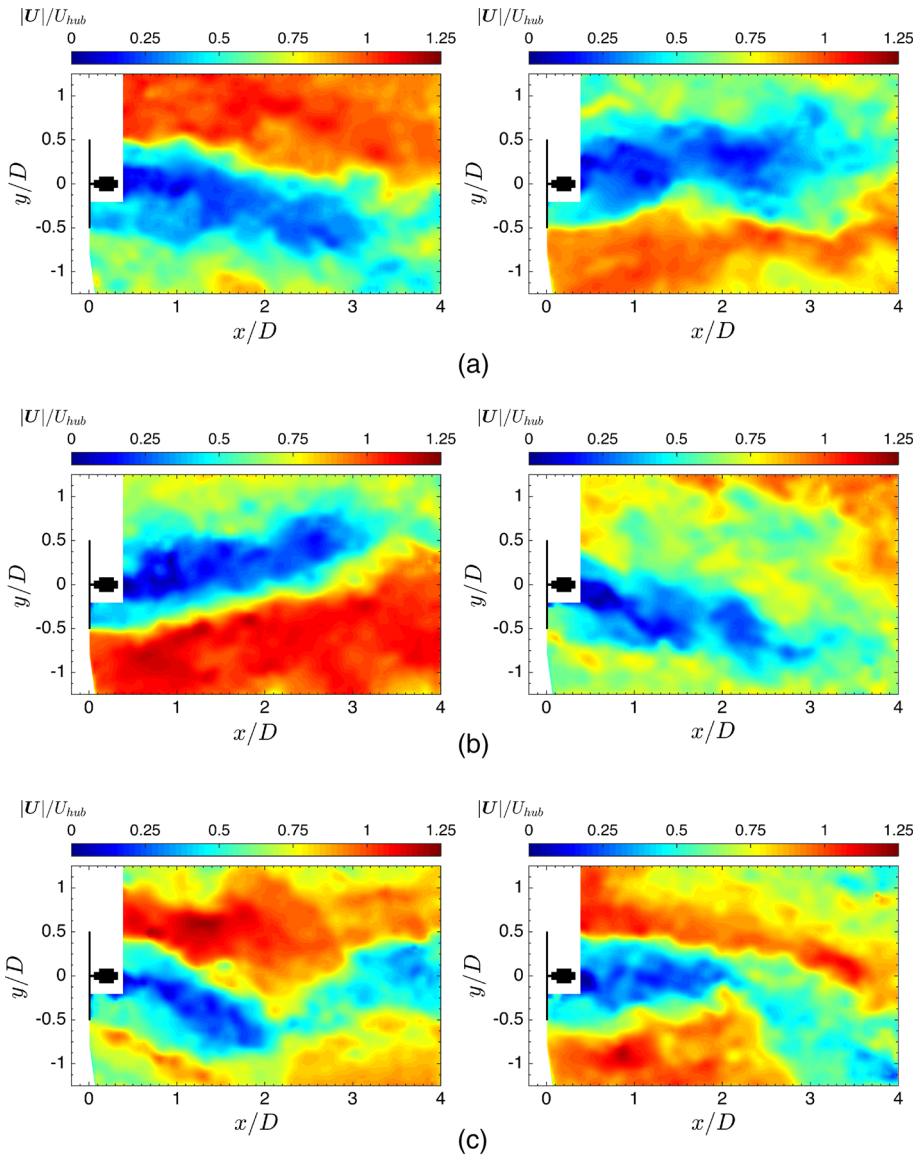


Fig. 10 Normalized instantaneous velocity fields at hub height at three different times revealing the asymmetrical impact of the upstream wake on the rotor of downstream turbines (a, b), and a possible interaction between the wakes of the lateral rows and the wakes of the central row (c) for the second (left) and third turbine (right)

$St \approx 0.25$ and $f/f_T \approx 0.09$ obtained in the experiments of Barlas et al. (2015, 2016). Also consistent with Barlas et al. (2015, 2016) is the independence of the Strouhal number of the meandering phenomenon from the incoming flow speed. Note that the meandering wavelength ($\lambda = D/St$) is $\approx 4.5D - 4.75D$, thus justifying the large field-of-view required for the PIV measurements.

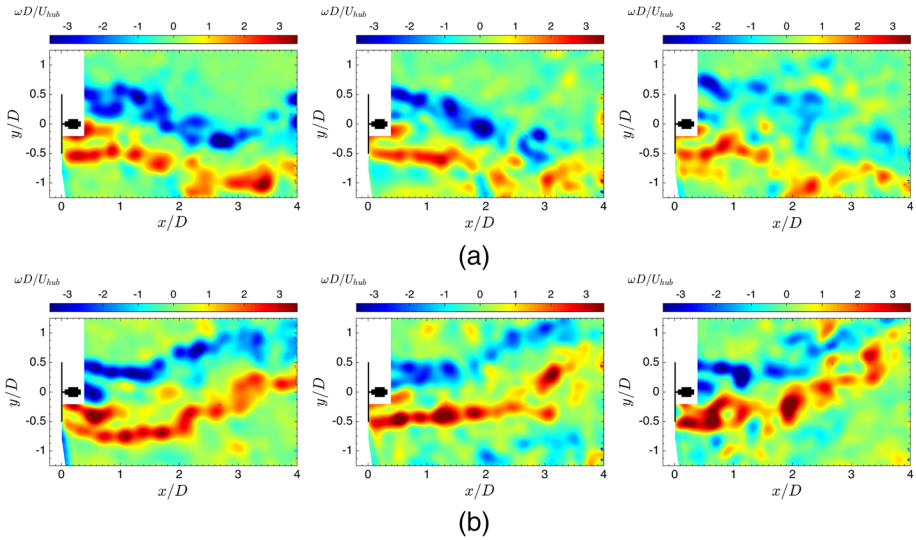


Fig. 11 Normalized instantaneous vorticity fields at hub height at two different times **(a, b)** revealing wake deflection for the first (left), second (centre) and third (right) turbines

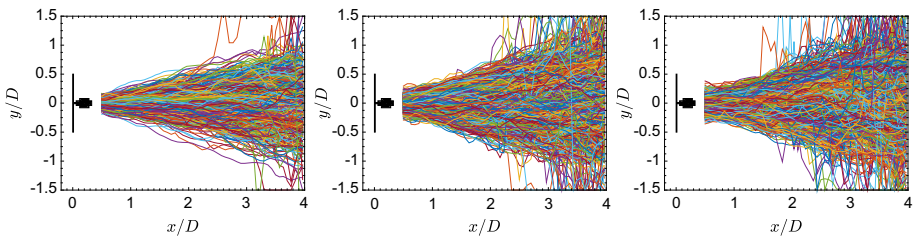


Fig. 12 Normalized wake-centre positions at hub height as a function of the streamwise position for each instantaneous velocity field for the first (left), second (centre) and third (right) turbines

Table 2 The rotational frequency f_T of the wind-turbine scale models

U_{hub} (m s ⁻¹)	f_T (Hz)		
	WT1	WT2	WT3
4.9	66.7	51.5	54.6
8.3	127.2	102.9	105.1

To validate the concept of our wake-centre algorithm, the meandering characteristics obtained from PIV measurements (spatial approach) at hub height are compared with those obtained with hot-wire anemometry (temporal approach) at $x = 2D$, and at the same height (see Sect. 4.2). While the results agree well, particularly for the second and third turbines (Table 3), the comparison of the first wind-turbine wake is slightly worse because Taylor’s frozen turbulence hypothesis is probably less valid at the origin of the wake meandering. Nevertheless, the general excellent agreement between the two techniques provides an excellent validation of the wake-centre algorithm.

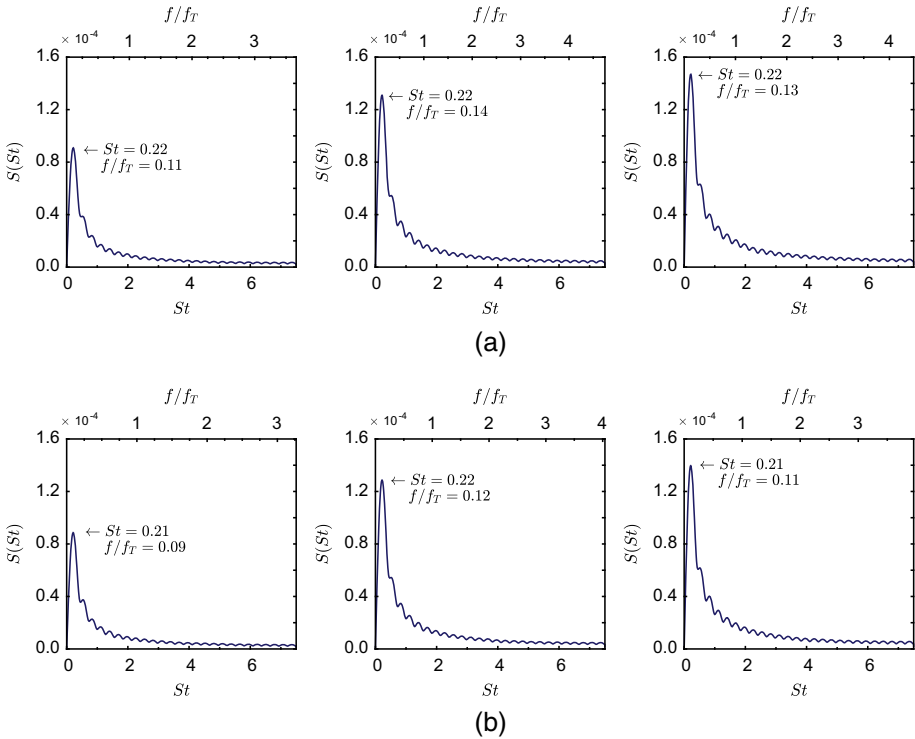


Fig. 13 Average zero-padded spectra of the wake-centre position at hub height for $U_{hub} = 4.9 \text{ m s}^{-1}$ (a) and $U_{hub} = 8.3 \text{ m s}^{-1}$ (b) for the first (left), second (centre) and third (right) turbines

Table 3 Meandering characteristics, Strouhal number and frequency normalized by the rotor rotational frequency f_T , obtained with PIV and hot-wire anemometry at hub height

	U_{hub} (m s ⁻¹)	WT1		WT2		WT3	
		St	f/f_T	St	f/f_T	St	f/f_T
PIV	4.9	0.22	0.11	0.22	0.14	0.22	0.13
	8.3	0.21	0.09	0.22	0.12	0.21	0.11
HWA	7.8	0.14	0.06	0.22	0.11	0.20	0.10

4.2 Spectral Wake Characteristics from Hot-Wire-Anemometry Measurements

Figure 14 enables comparison of the energy spectrum of the inflow with that at $x = 2D$ in the wake of the turbines in the middle row for heights of $z/z_{tip} = 1.4$, $z/z_{tip} = 1$, $z/z_{hub} = 1$, and $z/z_{tip} = 0.2$, where energy appears clearly larger in the wake than in the inflow. In contrast to Barlas et al. (2015, 2016), the energy spectra acquired in the wakes do not present a well-pronounced narrow peak at low frequency, but rather an elongated peak spread over a larger low-frequency range, especially at tip height. Furthermore, the peak corresponding to the rotational frequency of the rotor obtained at tip height in Barlas et al. (2015, 2016) is not visible here. As discussed previously, the differences observed most probably result from the higher turbulence intensity of the inflow ($I = 10.5\%$ here, $I = 7.5\%$ in Barlas et al. (2015, 2016) at hub height). As with the PIV results, the hot-wire-anemometry results show

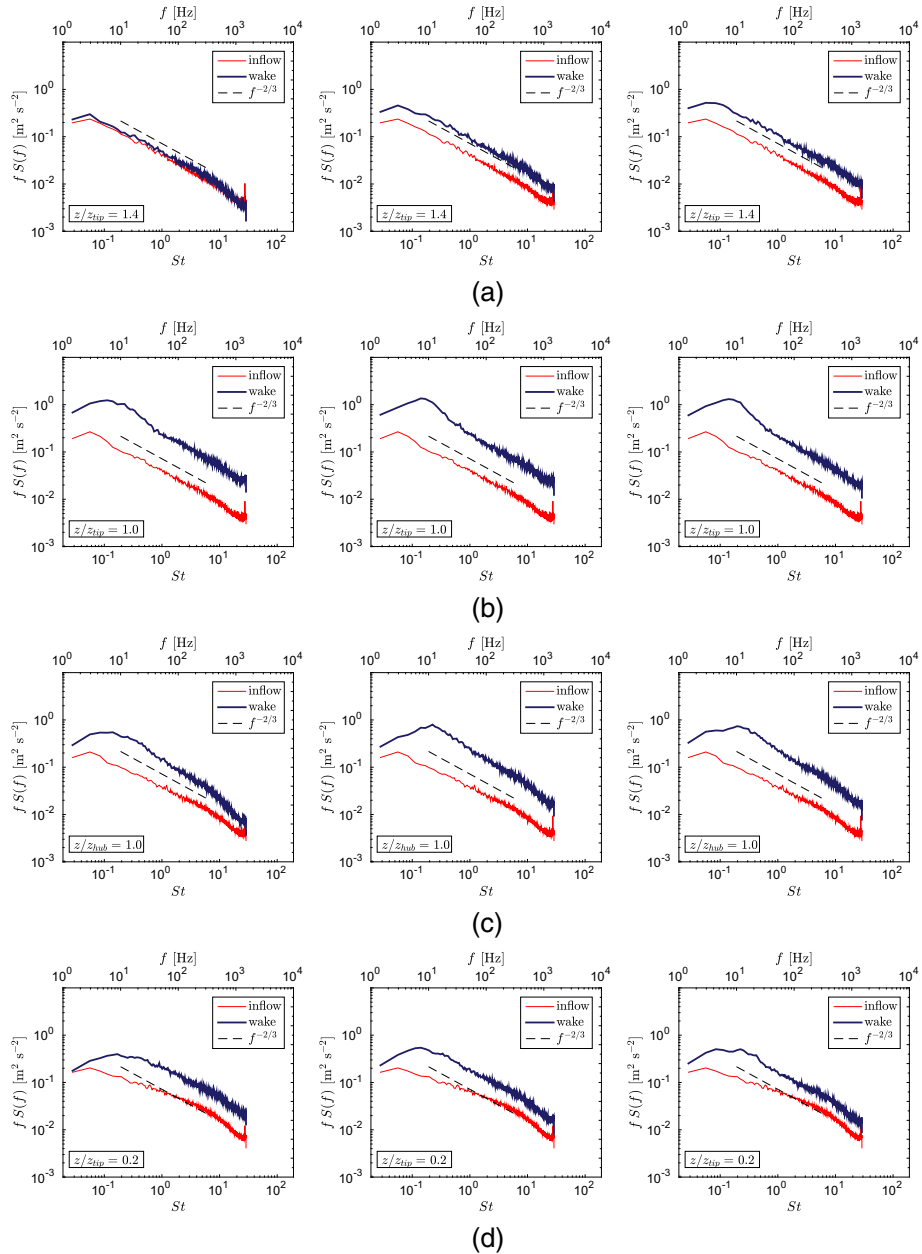


Fig. 14 Comparison of the energy spectra of the inflow with that at $x = 2D$ at $z/z_{tip} = 1.4$ (a), $z/z_{tip} = 1$ (b), $z/z_{hub} = 1$ (c), and $z/z_{tip} = 0.2$ (d) for the first (left), second (centre) and third (right) turbines

that, in contrast to [Barlas et al. \(2015\)](#), the meandering phenomenon persists within the wind farm. Note that, even if the spectra presented in [Barlas et al. \(2015, 2016\)](#) were obtained at $x = 1D$, the peaks would even be more pronounced at $x = 2D$ when considering the spectrograms presented in [Barlas et al. \(2015, 2016\)](#).

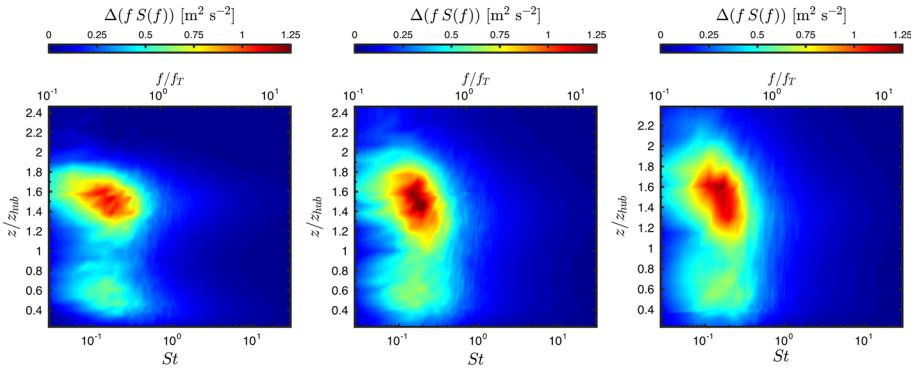


Fig. 15 Differential energy spectra between the wake and the inflow spectra for different heights at $x = 2D$ for the first (left), second (centre) and third (right) turbines. Here, $I = 10.5\%$ in the boundary-layer inflow

Energy spectra for the wake and inflow at $x = 2D$ (Fig. 15) show a peak at $f/f_T \approx 0.07$ ($St \approx 0.17$), $f/f_T \approx 0.10$ ($St \approx 0.2$), and $f/f_T \approx 0.08$ ($St \approx 0.17$) for the first, second and third turbines, respectively. Both the spectrograms presented in Barlas et al. (2015, 2016) and the spectrogram of the first turbine (Fig. 15) show a peak at around $f/f_T \approx 0.09$. As stated for the spectra at hub height, our spectrograms give a peak spread over a larger low-frequency range than those presented in Barlas et al. (2015, 2016). Furthermore, the peak is centred here around the upper-tip height, but around the hub height in the results of Barlas et al. (2015, 2016). In addition, while the turbine rotational frequency is visible in the spectrograms of Barlas et al. (2016), it is not visible here. As above, such results can be explained by the difference in boundary-layer turbulence intensity.

5 Discussion and Conclusion

The wake-meandering phenomenon has been investigated experimentally within a 3×3 scaled wind farm placed in the neutral boundary layer of a wind tunnel, corresponding to an ABL with slightly rough terrain (offshore conditions). As the turbulence intensity at hub height is $I \approx 10.5\%$, and the integral length scale at hub height is $L \approx 3D$, the characteristic size of the energy-containing eddies fulfils the conditions specified in España et al. (2011, 2012) for ensuring the wake-meandering phenomenon. For this purpose, the modelled turbulent scales must be larger than the turbine rotor diameter in the inflow. With a rotor diameter of 0.15 m and a hub height of 0.13 m, the models are representative of scaled 2-MW offshore wind turbines (e.g. a scale 1/440 of a Vestas V66-2MW).

Particle-image-velocimetry (PIV) measurements were performed in a horizontal plane located at hub height in the wake of the three turbines of the middle row (in the streamwise direction) of the scaled wind farm. The meandering phenomenon is clearly visible in the wake of the turbines. From the PIV measurements, a good estimate of the instantaneous wake-centre position as a function of the streamwise location is obtained by tracking the maximum value of a fitted Gaussian profile to the instantaneous velocity deficit for each position in the wake. For each wake-centre-position curve and after subtraction of the mean position, a zero-padded fast Fourier transform is applied to obtain the frequency characteristics of the wake-meandering phenomenon. In contrast to what has previously been observed (Barlas et al. 2015), the wake-meandering phenomenon persists within the scaled wind farm, and

is clearly visible in the instantaneous velocity fields for each of the three turbines in a row. In addition to the PIV technique, hot-wire anemometry was performed at $x = 2D$ in the wake of the turbines to support the conclusions drawn in [Barlas et al. \(2015, 2016\)](#). The measurements show a correct spectral behaviour with regard to the expected $-2/3$ slope. As with the PIV results, the hot-wire-anemometry results show that the meandering phenomenon persists in the scaled wind farm, and is clearly still present beyond the first two rows. The different meandering behaviours observed inside the wind farm could be due to the differences between the two experimental campaigns, i.e. (i) the wind-turbine rotor, (ii) the tip-speed ratio, and (iii) the boundary-layer properties. We argue that neither the differences between the two rotors nor the different tip-speed ratios explain the different meandering behaviours, since our tip-speed ratios fall into the range of tip-speed ratios for which [Barlas et al. \(2015, 2016\)](#) have observed wake meandering with Strouhal numbers ≈ 0.25 . The differences are most probably due to the higher turbulence intensity of our boundary layer ($I = 10.5\%$ at hub height) compared with that ($I = 7.5\%$ at hub height) of [Barlas et al. \(2015, 2016\)](#). The major influence of the turbulence intensity is reinforced by the fact that, in the experiments of [Barlas et al. \(2015, 2016\)](#), the absence of meandering was observed in the wake of a single turbine located in a rough-terrain boundary layer, resulting in a very high turbulence intensity, $I = 17.5\%$ at hub height.

Even if the PIV system employed is unable to resolve in time wake meandering given its characteristic frequency of 10–15 Hz, the large field-of-view of the PIV camera make it possible to perform a spatial analysis of the meandering structure from the acquired PIV velocity fields. That the Strouhal numbers obtained from hot-wire anemometry ($St = fD/U_{hub}$) and PIV ($St = D/\lambda$) are both $St \approx 0.20 - 0.22$ proves the validity of Taylor's frozen turbulence hypothesis for identification of the wake-meandering phenomenon. Our results fall into the range of Strouhal numbers obtained by [Medici and Alfredsson \(2008\)](#) for their study of the influence of the number of blades, the blade pitch angle and the tip-speed ratio on the frequency of wind-turbine-wake meandering. Indeed, the measurements performed in the near wake ($x/D = 1$) of a three-bladed model show that the Strouhal number may vary from 0.15 to 0.3 depending on the operating conditions. Wake oscillations at low frequencies corresponding to Strouhal numbers falling into this range have also been observed in other studies. Indeed, acoustic Doppler velocimetry performed in the wake of a hydrokinetic turbine located in a turbulent boundary layer reveal that the wake shows a strong lateral periodic motion at low frequency corresponding to $St = 0.28$ at $x/D = 4$ ([Chamorro et al. 2013](#)). From laser Doppler anemometry performed in the wake of a three-bladed wind-turbine rotor mounted on a long arm and located in a water flume with a homogeneous freestream velocity and 2% turbulence intensity, [Okulov et al. \(2014\)](#) reported that the wake oscillates periodically with $St \approx 0.23$, independent of the operating conditions. Finally, [Howard et al. \(2015\)](#) observed wake meandering at $St \approx 0.3$ for a wind-turbine scale model operating at an optimal tip-speed ratio in a boundary layer corresponding to slightly rough terrain.

Nevertheless, in providing experimental evidence of the role of large-scale turbulent eddies on wake meandering, [España et al. \(2012\)](#) could not obtain a typical Strouhal number from hot-wire-anemometry measurements performed at $x/D = 3$ behind a wind turbine modelled by a porous disk and placed in a boundary layer corresponding to a moderately-rough terrain. After collecting evidence for the presence of wake meandering behind the porous disk, they argued that the meandering phenomenon cannot be attributed to periodic vortex shedding, since the wake oscillations are without any periodicity.

The formation of wind-turbine-wake meandering seems to be neither entirely due to the intrinsic instabilities of the wake associated with a periodic vortex shedding, nor entirely due to the effects of the large-scale turbulent eddies contained in the ABL as observed for

plume-dispersion analysis. Rather, the wake-meandering formation appears to be due to a combination of both of these mechanisms. Indeed, the Strouhal number obtained is in favour of the role of intrinsic instabilities of the wake, and that meandering does not appear for integral length scales smaller than the rotor diameter (España et al. 2012) underlines the influence of large-scale eddies within the ABL. The formation of wake meandering appears, therefore, to be caused by the amplification of the intrinsic instabilities of the wake by large-scale turbulent eddies within the ABL.

While the perspectives of our study are many, the influence of the terrain roughness and atmospheric stability, as well as the influence of the wind-turbine operating conditions on the wake-meandering phenomenon, require further investigation. Furthermore, since several of the velocity fields obtained reveal a possible lateral interaction between the wakes of the lateral rows and those of the central row, we are planning further PIV measurements, with a field-of-view including the wakes of two laterally adjacent wind-turbine models, for the study of this possible interaction.

Acknowledgements Nicolas Coudou was supported by a fellowship of the Belgian FRIA F.R.S-FNRS for part of this work.

Appendix 1

See Table 4.

Table 4 Wind-turbine blade characteristics for the chord length (c) and pitch angle (β) as a function of the distance from the turbine axis (r). Here, $R = D/2$

r/R	0.067	0.100	0.133	0.167	0.200	0.233	0.267	0.300	0.333	0.367
c/R	0.334	0.326	0.319	0.311	0.303	0.295	0.287	0.279	0.271	0.263
β [°]	21.1	21.7	20.3	19.0	17.8	16.7	15.6	14.7	13.8	12.9
	0.400	0.433	0.467	0.500	0.533	0.567	0.600	0.633	0.667	0.700
	0.256	0.248	0.240	0.232	0.224	0.216	0.208	0.201	0.193	0.185
	12.1	11.4	10.7	10.1	9.5	9.0	8.4	8.0	7.5	7.0
	0.733	0.767	0.800	0.833	0.867	0.900	0.933	0.967	1.000	
	0.177	0.169	0.161	0.153	0.146	0.138	0.130	0.122	0.114	
	6.6	6.2	5.7	5.3	4.9	4.5	4.0	3.6	3.1	

References

- Anthoine J, Arts J, et al (1994) Measurements techniques in fluid dynamics: an introduction. Von Karman Institute for Fluid Dynamics, Reprint of VKI LS 1994-01, Third revised edition, pp 8–10
- Aubrun S, Loyer S, España G, Hayden P, Hancock P (2011) Experimental study on the wind turbine wake meandering with the help of a non-rotating simplified model and of a rotating model. Orlando, FL, AIAA 2011-0460, 49th AIAA aerospace sciences meeting
- Aubrun S, Tchouaké TF, España G, Larsen G, Mann J, Bingöl F (2012) Progress in turbulence and wind energy IV: proceedings of the iTi conference in Turbulence 2010. Springer, Berlin

- Aubrun S, Muller YA, Masson C (2015) Predicting wake meandering in real-time through instantaneous measurements of wind turbine load fluctuations. *J Phys Conf Ser* 625(1):012005
- Barlas E, Buckingham S, Glabeke G, van Beeck J (2015) Offshore and onshore wind turbine wake meandering studied in an ABL wind tunnel. In: International workshop on physical modeling of flow and dispersion phenomena PHYSMOD). Zürich
- Barlas E, Buckingham S, van Beeck J (2016) Roughness effects on wind-turbine wake dynamics in a boundary-layer wind tunnel. *Boundary-Layer Meteorol* 158(1):27–42
- Bingöl F, Mann J, Larsen GC (2010) Light detection and ranging measurements of wake dynamics part I: one-dimensional scanning. *Wind Energy* 13(1):51–61
- Buckingham S (2010) Wind park siting in complex terrains assessed by wind tunnel simulations. PR 2010-04, von Karman Institute for Fluid Dynamics
- Burton T, Sharpe D, Jenkins N, Bossanyi E (2001) *Wind energy handbook*. Wiley, New York
- Chamorro L, Arndt R, Sotiropoulos F (2012) Reynolds number dependence of turbulence statistics in the wake of wind turbines. *Wind Energy* 15(5):733–742
- Chamorro LP, Hill C, Morton S, Ellis C, Arndt REA, Sotiropoulos F (2013) On the interaction between a turbulent open channel flow and an axial-flow turbine. *J Fluid Mech* 716:658–670
- Churchfield MJ, Lee S, Moriarty PJ, Hao Y, Lackner MA, Barthelmie R, Lundquist JK, Oxley G (2015) A comparison of the dynamic wake meandering model, large-eddy simulation, and field data at the Egmond aan Zee offshore wind plant. Kissimmee, FL, AIAA 2015-0724. In: 33rd wind energy symposium, AIAA SciTech
- Conan B (2012) Wind resource assessment in complex terrain by wind tunnel modelling. Ph.D. thesis, Université d'Orléans—von Karman Institute for Fluid Dynamics, VKI PHDT 2013-04
- Corbetta G, Ho A, Pineda I, Ruby K, Van de Velde L (2015) Wind energy scenarios for 2030. <http://www.ewea.org/fileadmin/files/library/publications/reports/EWEA-Wind-energy-scenarios-2030.pdf>. The European Wind Energy Association
- Corbetta G, Mbistrova A, Ho A, Pineda I, Ruby K (2016) Wind in power—2015 European statistics. <http://www.ewea.org/fileadmin/files/library/publications/statistics/EWEA-Annual-Statistics-2015.pdf>. The European Wind Energy Association
- ESDU (1985) Characteristics of atmospheric turbulence near the ground. Part II: single point data for strong winds (neutral atmosphere). Engineering Sciences Data Unit, London
- España G, Aubrun S, Loyer S, Devinant P (2011) Spatial study of the wake meandering using modelled wind turbines in a wind tunnel. *Wind Energy* 14(7):923–937
- España G, Aubrun S, Loyer S, Devinant P (2012) Wind tunnel study of the wake meandering downstream of a modelled wind turbine as an effect of large scale turbulent eddies. *J Wind Eng Ind Aerodyn* 101:24–33
- Eurocode (2005) EN 1991-1-4:2005: actions on structures—part 1-4: general actions—wind actions. CEN
- Howard KB, Singh A, Sotiropoulos F, Guala M (2015) On the statistics of wind turbine wake meandering: an experimental investigation. *Phys Fluids* 27(7):075103
- International Towing Tank Conference (2008) Recommended procedures and guidelines: uncertainty analysis—particle image velocimetry. 7.5-01-03-03
- Kaimal J, Finnigan J (1994) *Atmospheric boundary layer flows: their structure and measurement*. Oxford University Press, Oxford
- Larsen GC, Madsen HA, Thomsen K, Larsen TJ (2008) Wake meandering: a pragmatic approach. *Wind Energy* 11(4):377–395
- Medici D, Alfredsson PH (2006) Measurements on a wind turbine wake: 3D effects and bluff body vortex shedding. *Wind Energy* 9(3):219–236
- Medici D, Alfredsson PH (2008) Measurements behind model wind turbines: further evidence of wake meandering. *Wind Energy* 11(2):211–217
- Muller YA, Aubrun S, Masson C (2015) Determination of real-time predictors of the wind turbine wake meandering. *Exp Fluids* 56(3):1–11
- Okulov VL, Sørensen JN (2007) Stability of helical tip vortices in a rotor far wake. *J Fluid Mech* 576:1–25
- Okulov VL, Naumov IV, Mikkelsen RF, Kabardin IK, Sørensen JN (2014) A regular strouhal number for large-scale instability in the far wake of a rotor. *J Fluid Mech* 747:369–380
- Scarano F (2000) Particle image velocimetry—development and application. Ph.D. thesis, von Karman Institute for Fluid Dynamics, VKI PHDT 2000-06
- Sumer BM, Fredsøe J (1997) *Hydrodynamics around cylindrical structures*. World Scientific Publishing Co Pte Ltd, Singapore, pp 10–13
- VDI Guidelines 3783/12 (2000) Physical modelling of flow and dispersion processes in the atmospheric boundary layer—Application for wind tunnels. Beuth Verlag
- Vollmer L, Steinfeld G, Heinemann D, Kühn M (2016) Estimating the wake deflection downstream of a wind turbine in different atmospheric stabilities: an LES study. *Wind Energy Sci* 1(2):129–141